CrN electronic structure and vibrational modes: An optical analysis

X. Y. Zhang and D. Gall
Rensselaer Polytechnic Institute, Troy, New York 12180, USA
(Received 30 April 2010; revised manuscript received 18 June 2010; published 20 July 2010)

The optical properties of paramagnetic CrN over the wavelength range 250 nm–30 μm were determined from transmission and reflection spectra of 44–11 000-nm-thick epitaxial CrN(001) layers that were grown on MgO(001) by ultrahigh vacuum magnetron sputtering at 700 °C and were found to be pure cubic single crystals by x-ray diffraction ω-2θ, ω, and φ scan analyses. The imaginary part of the dielectric function exhibits a steep onset at $\hbar\omega$=0.64 eV as well as peaks at $\hbar\omega$=1.5 and 2.9 eV due to direct interband transitions and indicates a depletion in the density of states at the Fermi level with an upper limit for free carriers of 3×10^{19} cm^{-3}. This is attributed to local magnetic moments that cause splitting of the t_{2g} bands and the formation of an indirect band gap of 0.19 ± 0.46 eV, as estimated by comparing the optical transition energies with reported direct gap energies from calculations with different magnetic ordering and Coulomb interaction terms. The dielectric function shows a strong resonance at $\hbar\omega_0=48.7\pm0.2$ meV, and values of $\varepsilon_{dc}=53\pm5$ and $\varepsilon_\infty=22\pm2$ below and above the resonance, respectively, providing values for transverse and longitudinal optical phonon frequencies at the zone center of 11.7 THz and 18.2 THz (corresponding to $\hbar\omega=48.7\pm0.2$ and 75.6 ± 6.8 meV), respectively, and a Born effective charge of 4.4 ± 0.9. The vibrational frequencies are confirmed by Raman spectroscopy peaks at 800, 1170, and 1330 cm^{-1} which are attributed to 2TO(X), 2LO(X), and 2LO(L) modes and correspond to single-phonon energies of 49.6 meV, 72.5 meV, and 82.5 meV, respectively. They are quantitatively comparable to those reported for ScN, a semiconductor with the same crystal structure as cubic CrN. In conclusion, both electronic interband transitions and optical phonon frequencies suggest that CrN is a Mott-Hubbard-type insulator with a small to negligible indirect band gap.

DOI: 10.1103/PhysRevB.82.045116 PACS number(s): 78.20.Ci, 71.28.+d, 78.40.Ha, 78.30.Hv

I. INTRODUCTION

Chromium nitride (CrN) is well known for its high hardness and mechanical strength, corrosion resistance, chemical inertness, and high-temperature stability[1–3] and has therefore become an important material for protective and abrasion resistant coatings.[4–7] In addition, the electronic structure of CrN has recently gained considerable interest since a possible band gap in combination with magnetic ordering makes CrN a promising material for diluted magnetic semiconductors, in particular, in combination with (or dopant in) other nitride semiconductors.[8–10] However, no consensus has been reached regarding the electronic properties of CrN, with reported values for the room-temperature resistivity ρ ranging from 3×10^{-4} to 20 Ω cm,[8,11–22] with likely the most reliable data from single-crystal CrN layers within a narrower range of 8.2×10^{-2}–1.7×10^{-3} Ω cm.[8,16–18] The temperature dependence of ρ is also controversial, showing metallic behavior with $d\rho/dT>0$ in some studies,[17,18,20] but an increase in ρ with decreasing temperature in other reports,[8,11,16] which has been attributed to the presence of a band gap[16] or carrier localization due to grain boundaries[21] or N vacancies.[19] In addition, some reported $\rho(T)$ curves are monotonous[16] while others show a discontinuity at 260–280 K,[8,17–19] which is associated with a magnetic and structural phase transition with a Néel temperature T_N=273–286 K, from a paramagnetic NaCl structure above room temperature to a low-temperature antiferromagnetic (AFM) orthorhombic *Pnma* phase[20,23–25] with a 0.56–0.59 % increase in atomic density[20,25] and a 25% lower bulk modulus.[26] Electronic-structure calculations indicate that a distorted antiferromagnetic $[110]_2$ phase is energetically more stable than paramagnetic, ferromagnetic (FM), and antiferromagnetic $[110]_1$ CrN,[27,28] and magnetic stress relief couples magnetic ordering with the structural change during the phase transition,[29] which may also be induced by increasing the pressure above ~1 GPa.[26] Additionally, Herwadkar *et al.*[28] reported a depletion of electron states near the Fermi level and the opening of a band gap when using a Hubbard Coulomb interaction term U=3–5 eV, and concluded that CrN is close to a "charge-transfer insulator."

In summary, both experimental and theoretical approaches have not yet been able to resolve the question whether CrN is a metal or a semiconductor nor if and to what extent the magnetic ordering and the associated structural phase transition affects the possible band gap. We attribute this challenge in determining the CrN electronic structure on the theoretical side to difficulties in correctly accounting for electron correlation and electron interaction within density-functional approaches, leading to large uncertainties in band-gap values, and on the experimental side to N vacancies which are common in NaCl-structure nitrides such as ScN (Ref. 30) or TaN,[31] act as donors,[19] and may cause carrier localization,[28,31] but are difficult to quantify and vary with synthesis method. In addition, epitaxial constraints from the substrate may suppress the structural and, in turn, the magnetic phase transition.[9,18]

In this paper, we present the results of an investigation on the CrN electronic structure where we focus primarily on electronic interband transitions and on lattice vibrations, measured by optical spectroscopy. This approach is less sensitive to N vacancies than the above-mentioned studies that employ electron-transport measurements to determine the electronic structure. CrN layers were grown on MgO(001) at 700 °C by reactive magnetron sputtering and were found to

be good-quality single crystals by x-ray diffraction. The refractive index n and extinction coefficient k were determined by combining optical transmittance and reflectance over a large wavelength range 250 nm$\leq\lambda\leq$30 μm and for samples with thickness t=44–11 000 nm. Features in the dielectric function at 0.64, 1.5, and 2.9 eV indicate direct interband transitions which allow, when comparing with band-structure calculations, to estimate the fundamental indirect gap to be 0.19 ± 0.46 eV. This is consistent with the absence of free-carrier contributions over the entire measurement range, indicating a carrier density $\leq 3\times10^{19}$ cm^{-3}. The combination of infrared reflectivity and Raman spectroscopy provides CrN optical vibrational frequencies at various points in the Brillouin zone, and Born effective charges of $\pm$4.4 for Cr and N ions, confirming the low free-carrier concentration. The qualitative and quantitative similarities of the dielectric function and the phonon dispersion curves of CrN with those reported for ScN, which is a semiconducting NaCl-structure nitride,[32] are also consistent with the presence of a band gap in CrN.

II. EXPERIMENTAL PROCEDURE AND OPTICAL ANALYSIS METHOD

All CrN layers were grown in a load-locked ultrahigh vacuum dc magnetron sputtering system,[33] with a base pressure of 1.3×10^{-7} Pa (1×10^{9} Torr), onto two-side polished $20\times20\times0.5$ mm^3 MgO(001) wafers that were cleaned, mounted, and degassed for epitaxial growth as described in Ref. 34. Deposition was performed at a substrate temperature of 700 °C in 0.39 Pa (3 mTorr) 99.999% pure N_2 that was further purified through a Micro Torr purifier. A 5-cm-diameter 99.95% pure Cr target was positioned 10.5 cm from the substrate at an angle of 45°, and a constant magnetron power of 350 W was applied, yielding a growth rate of 22 nm/min, as determined from thickness measurements by Rutherford backscattering spectroscopy (RBS). These deposition conditions are expected to yield stoichiometric CrN with a N:Cr ratio of 1.00 ± 0.06, based on our previous studies,[16,22] and consistent with RBS results from calibration samples. The surface roughness is expected to increase with thickness but to be always less than 5% of the layer thickness, based on *in situ* scanning tunneling microscopy and atomic force microscopy studies on CrN layers deposited in the same deposition system.[35,36]

The layer microstructure was investigated by x-ray diffraction (XRD) ω-2θ, ω rocking curve, and φ scans in a Bruker D8 diffractometer with a Cu $K\alpha$ source ($\lambda_{K\alpha1}$ =1.5406 Å, $\lambda_{K\alpha2}$=1.5444 Å) equipped with a Goebel x-ray mirror yielding a parallel beam with a divergence $<$0.028°. Optical transmittance and reflectance spectra were obtained over the wavelength range λ=250–2500 nm using a Perkin-Elmer Lambda 950 spectrophotometer and between 5000 and 334 cm^{-1}, corresponding to λ=2–30 μm, using a Nicolet Magna IR-560 Fourier transform infrared (FTIR) spectrometer. Transmittance was measured with normal incident light while the incident angle for reflectance measurements was 6° for the spectrophotometer and 45° for the FTIR spectrometer. Raman spectra were obtained using a Renishaw Raman microscope 2000 system with a diode laser which provides a 50 mW beam with a wavelength of 785 nm. The primary laser beam passes through the same 50X objective lens that is used to collect the reflected and scattered light, which passes through a dielectric Rayleigh filter before being dispersed by a diffraction grating onto a charge coupled device camera.

The refractive index n and extinction coefficient k for CrN are determined from the measured optical reflectance spectrum from the thickest sample with t=11 000 nm, and from a set of transmittance spectra with t=44, 220, 1100, 2200, and 11 000 nm. This analysis approach circumvents the often challenging optical fitting procedure that is sensitive to surface and interface roughness and oxidation, as well as thickness variations. In particular, the measured R for t =11 000 nm is unaffected ($<$0.01%) by reflections at the backside, i.e., the CrN-MgO interface, over the entire wavelength range, as the layer is sufficiently thick to absorb the light during two paths through the CrN. Also, for transmission data, different sample thicknesses are used for different spectral ranges such that most of the intensity is absorbed in the first path through the layer, that is $10^{-3}<T<10^{-1}$. Under such "high-absorption" conditions, the absorption coefficient α depends only logarithmically on the measured transmission[37] and is therefore relatively insensitive to uncertainties in correctly accounting for surface effects, including roughness, oxidation, and surface-near density variations, as well as to experimental calibration errors, which are estimated to be 3–10 %, but only cause an uncertainty in α of 1%. An iterative procedure is employed to determine n and k, as follows. The absorption coefficient α, and, in turn, the extinction coefficient $k=\lambda/4\pi\times\alpha$, is obtained from the measured T by accounting for multiple coherent reflections[38] at the air-CrN and CrN-MgO interfaces as well as the absorption in the substrate, using n and k for CrN from the previous iteration step and the optical constants for MgO, obtained from T and R measurements on a bare substrate, which are in good agreement with the MgO optical constants in Palik's handbook.[39] In the second iterative step, n is obtained from the measured R, keeping k constant. Convergence is relatively rapid, since T ($<$0.1) depends primarily on the absorption in the layer, while R depends more strongly on n than k, since $n>k$ in our experiments. To simplify the formalism, the following approximations are employed which introduce less than 2% and 0.1% errors in k and n, respectively. (i) Fresnel's equation for normal incidence is used to describe the measured R with a 6° incidence angle, since it is accurate to within $<$1% for the spectrophotometer wavelength range. The 45° incident angle is correctly accounted for in the FTIR wavelength range of 2–30 μm. (ii) The reflection at the MgO-air interface has been neglected, which is a $<$8% reflection that affects T by $<$3%, which is below the experimental calibration uncertainty of up to 10%.

The n and k for $3<\lambda<30$ μm are obtained from a Kramers-Kronig (KK) analysis,[40,41] using the normal-polarization reflectance R_s data from a 45° incidence angle for λ=2–30 μm. This is done in order to determine the optical constants particularly for $\lambda>11$ μm, where the transmittance cannot be measured due to the strong absorption in the MgO substrate.

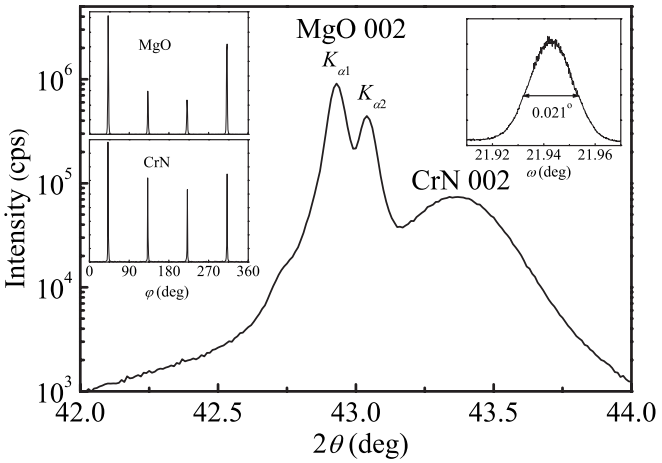

FIG. 1. XRD ω-2θ scan from a 2-μm-thick CrN/MgO(001) sample. Insets show corresponding φ scans for MgO 111 and CrN 111 reflections, and an ω-rocking curve for the CrN 002 reflection at 2θ=43.36°.

III. RESULTS

Figure 1 shows XRD results from a 2.0-μm-thick CrN/MgO(001) layer which is representative for all samples in this study. The only peaks that are detected in a ω-2θ scan from 2θ=20° to 60° are MgO 002 and CrN 002 reflections, which are plotted in a log scale in Fig. 1. The MgO 002 reflection results in a double peak feature at 2θ=42.92° and 43.02°, associated with the characteristic $K\alpha1$ and $K\alpha2$ lines of the x-ray source, and corresponding to a lattice constant of 0.4211 nm, close to the literature value of 0.4212 nm (Ref. 42) or 0.4213 nm.[43] The two Cu lines cannot be resolved for the slightly broader and ~10× weaker CrN 002 peak at 2θ=43.36°. Using a weighted average source wavelength of 1.5418 Å, we calculate an out-of-plane CrN lattice constant of 0.4174 nm, which is in the range of reported bulk values 0.4133–0.4185 nm[17,22,44–46] but likely indicates a slight compressive strain due to differential thermal contraction during cooling from the 700 °C growth temperature, similar to what has been previously reported for epitaxial CrN grown on MgO(001).[22]

The right inset shows a corresponding ω-rocking curve of the CrN 002 peak at a constant 2θ=43.36°. The full width at half maximum is 0.021°, which is as narrow as the divergence of the x-ray source. That is, this value only provides an upper bound for the "true" rocking curve width of this CrN layer, which may therefore even be below 0.021°. This value is 4× and 7× lower than previously reported values for epitaxial CrN,[16,17] indicating the excellent crystalline quality of the CrN in this study and, in combination with φ scans, the absence of wide-angle grain boundaries. XRD scans about the azimuthal direction φ, obtained in the parallel-beam mode with ω and 2θ angles optimized for the 111 peak of MgO and CrN at a tilt angle of 54.7° with respect to the surface normal, exhibit four 90° rotated 111 peaks at the same angular positions φ=45°, 135°, 225°, and 315° for both MgO and CrN, shown in the left inset in Fig. 1. Therefore, the CrN layer is a complete single crystal, with a cube-on-cube epitaxial relationship with the substrate,

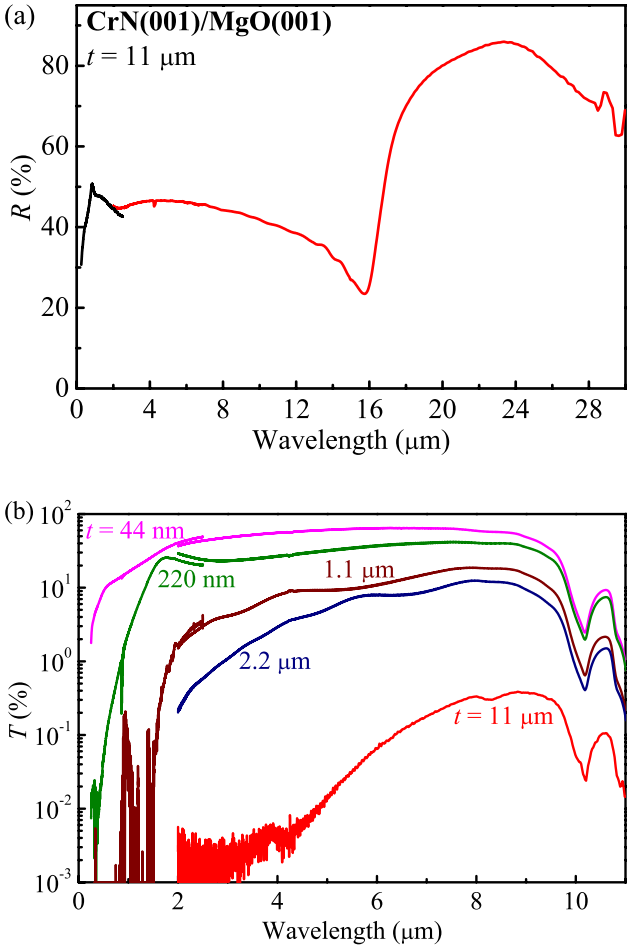

FIG. 2. (Color online) (a) Optical reflectance R from a nearly opaque 11-μm-thick CrN/MgO(001) layer measured with incident angles of 6° for $\lambda<2.5$ μm and 45° for $\lambda>2$ μm using a spectrophotometer and a FTIR spectrometer, respectively. (b) Normal optical transmittance T for CrN/MgO(001) layers with thicknesses t=0.044, 0.22, 1.1, 2.2, and 11 μm.

$(001)_{CrN}\|(001)_{MgO}$ and $[001]_{CrN}\|[001]_{MgO}$, similar to what has previously been reported for CrN (Refs. 47 and 48) as well as other transition-metal nitrides.[30,49–51]

Figure 2(a) shows the reflectance of CrN(001) for the entire measured wavelength range, 0.25–30 μm. The plot consists of two separate curves for $\lambda<2.5$ μm and $\lambda>2$ μm measured by the spectrophotometer and FTIR, respectively. The slight 1% intensity difference at $\lambda=2$ μm from the two separate measurements is due to the different incidence angles 6° and 45°, respectively, as well as to instrument calibration uncertainty. The curve is from the thickest sample in this study, t=11 μm, which renders reflections from the sample backside negligible and is therefore most suited for the optical analysis below. The reflectance exhibits peaks at 0.85 and 23.4 μm, associated with electronic interband transitions and lattice vibrations, respectively, as discussed in detail below. The additional features above 28 μm may be attributed to anharmonic effects that lead to a relatively sharp subsidiary peak at λ=28.8 μm,[52] similar to what has been reported for alkali halides[53] and MgO.[54] The reflectance spectra from the thinner samples (not shown) exhibit the

same features but also interference fringes and substrate affects because a considerable fraction of the light intensity can pass through these thinner CrN layers.

Figure 2(b) is a semilog plot of the transmittance of CrN/MgO(001) layers with CrN thickness t=44, 220, 1100, 2200, and 11 000 nm, as labeled. The transmittance T increases for all samples monotonically from λ=0.25 to ~8 μm, followed by a decrease for $\lambda>8$ and negligible transmission for $\lambda>11$ μm. While the low transmission at low λ is due to absorption in the CrN, both the minimum in T centered at λ=10.2 μm as well as the T=0 above 11 μm are due to absorption in the MgO substrate, as quantified with a separate substrate-only measurement (not shown). As expected, transmittance is highest for the thinnest sample, increasing from 0.28% at λ=250 nm to 64% at λ=6 μm, but decreases as the sample thickness is increased, because an increasing fraction of the light intensity is absorbed in the CrN layer. For example, at λ=6 μm, T decreases from 64% to 37%, 11%, 7.9%, and 0.065% for t=44 nm, 220 nm, 1100 nm, 2200 nm, and 11 000 nm, respectively. Also, at low λ, where absorption in CrN is high, the transmission signal is too low to be measured, as evident by the noise in the plotted curves or the absence of curves at low λ in Fig. 2(b). The spectra also illustrate some experimental artifacts including the data scatter at λ=4.2–4.4 μm and at λ=860 nm, attributed to carbon dioxide absorption and the change in the spectrometer light source, respectively, as well as a discontinuity/overlap at λ=2–2.5 μm from the change in spectrometer, indicating spectrometer calibration and sample-to-sample uncertainties, which are estimated to be up to 10%, for all experiments presented here.

Figure 3 shows the result of the optical analysis from the R and T data. The absorption coefficient α is plotted in Fig. 3(a) vs the wavelength for the CrN/MgO(001) samples with different thickness t=44, 220, 1100, 2200, and 11 000 nm, as labeled in the plot. It is obtained using the iterative method described in the previous section, which accounts for multiple internal reflections but is particularly accurate in the regime where most of the light is absorbed in the first pass through the CrN layer, that is, where the measured T is small but still reliable. Correspondingly, the thick layers with t=2.2 and 11 μm are used to determine α in the FTIR range $2<\lambda<11$ μm, while the other three (thinner) layers are used in the spectrophotometer range, $250<\lambda<2500$ nm, where α is considerably higher. The continuous line through the data in Fig. 3(a) represents the overall result of the absorption analysis, obtained by combining the measured α from the different samples, as follows. At high $\lambda>5$ μm, absorption is low and the most reliable data is obtained from the thickest 11-μm-thick layer. The α from the next thinner sample with t=2.2 μm shows quantitative agreement. However, the data oscillate around the correct value since the higher transmittance of this sample results in interference effects which exacerbate errors due to sample thickness variations and interface roughness. In contrast, for $\lambda<4$ μm the absorption is sufficient that the t=2.2 μm curve becomes reliable while, at the same time, the measured T for t=11 μm is so low that α from the thickest layer is no longer reliable, as evident from the noise in the data in Fig. 2(b). Therefore, the "composite" α is obtained from t=2.2 μm for λ=2–4 μm and from t=11 μm for λ=5–11 μm, while the values are interpolated between λ=4 and 5 μm. A similar procedure is followed in the spectrophotometer wavelength range, where the absorption coefficient increases rapidly with decreasing wavelength from $\alpha=2.8\times10^4$ cm^{-1} at λ=2 μm to $\alpha=7.0\times10^5$ cm^{-1} at λ=250 nm. Therefore, the thinnest sample (t=44 nm) yields the most reliable α for $\lambda<860$ nm while t=220 nm is used for $860<\lambda<1500$ nm and t=1.1 μm for $1500<\lambda<2500$ nm. The plotted data are consistent with Ref. 16, which reported α for CrN over only a limited wavelength range 1–1.7 μm but showed the same steep increase and excellent quantitative agreement (within 10%) with the present study.

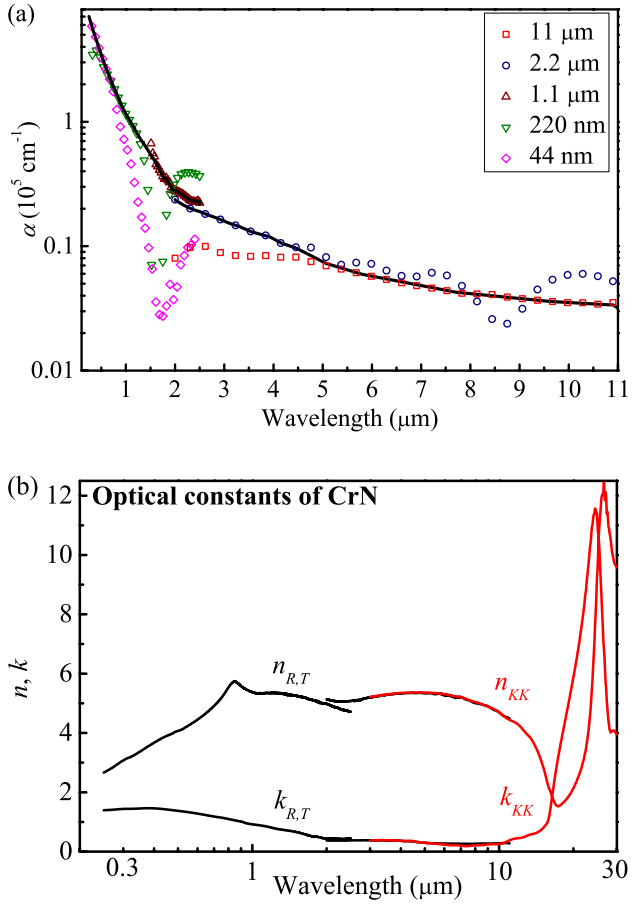

FIG. 3. (Color online) (a) The absorption coefficient α for CrN. The plotted data points are the result from the optical analysis using T data from layers with different thicknesses t=0.044, 0.22, 1.1, 2.2, and 11 μm, which are valid only over a limited wavelength range, while the continuous curve is the overall result. (b) Refractive index n and extinction coefficient k for CrN, determined for $0.25<\lambda<11$ μm using reflection and transmission data and for $3<\lambda<30$ μm using a Kramers-Kronig analysis.

Figure 3(b) is a plot of the CrN optical constants n and k vs the wavelength λ=0.25–30 μm. In the range where the substrate is at least partially transparent, that is $\lambda<11$ μm, the values were obtained from the same iterative procedure used to determine α. For this plot, k is obtained from the "composite" α shown in Fig. 3(a) while the n is directly

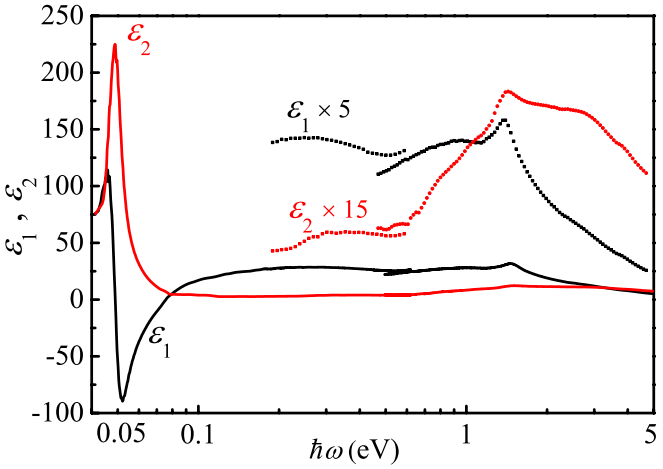

FIG. 4. (Color online) Real ε_1 and imaginary ε_2 parts of the CrN dielectric function.

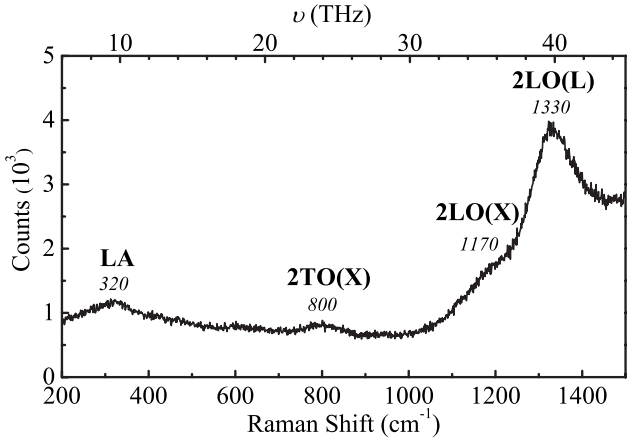

FIG. 5. Raman spectrum from a 11-μm-thick CrN(001) layer.

obtained from this k and the measured R of the thickest sample. Figure 3(b) also shows the n and k values from the KK analysis of the reflection spectrum for $\lambda=3-30$ μm. In the wavelength range $\lambda=3-11$ μm, the results from both analysis methods are plotted. However, the two lines can barely be distinguished in Fig. 3(b), as there is excellent agreement between them. In contrast, the imperfect overlap for $\lambda=2-2.5$ μm due to the measurements with two different spectrometers is still clearly visible in Fig. 3(b) and provides some indication of the overall uncertainty due to measurement calibration.

The refractive index continuously increases from $n=2.7$ at $\lambda=250$ nm to a peak of $n=5.7$ at $\lambda=840$ nm, followed by a nearly constant value of $n=5.2$ between $\lambda=1.2$ and 6.2 μm and a peak in the infrared where n reaches 12.4 at $\lambda=26.6$ μm, corresponding to a photon energy of 46.6 meV. The extinction coefficient increases slightly from 1.4 at $\lambda=250$ nm to 1.5 at $\lambda=390$ nm, followed by a drop to $k=0.5$ at $\lambda=1.8$ μm and a gentle decrease to $k=0.3$ at $\lambda=10$ μm. It exhibits a peak of $k=11.6$ at $\lambda=24.5$ μm, corresponding to a photon energy of 50.6 meV.

Figure 4 shows real ε_1 and imaginary ε_2 parts of the dielectric function vs photon energy $\hbar\omega=0.04-5$ eV, as directly calculated from n and k in Fig. 3(b). The imaginary part exhibits a strong bell-shaped symmetric peak at $\hbar\omega=48.7$ meV where ε_2 reaches 225. It remains relatively low with $\varepsilon_2=2.8-4.4$ between 0.2 and 0.64 eV, increases to reach a peak of $\varepsilon_2=12.3$ at 1.5 eV, exhibits a shoulder around $\hbar\omega=2.9$ eV, and decreases to reach $\varepsilon_2=0.49$ at 4.96 eV. The real part shows a strong resonance with a maximum of $\varepsilon_1=114$ and minimum of $\varepsilon_1=-90$ at $\hbar\omega=0.0459$ eV and 0.0521 eV, respectively, remains relatively constant with $\varepsilon_1=27.7-24.6$ between 0.1 and 0.64 eV, exhibits a peak with $\varepsilon_1=32$ at $\hbar\omega=1.46$ eV, and decreases continuously to 5.2 at 4.96 eV.

Figure 5 shows the Raman spectrum between 200 and 1500 cm^{-1} from a 11-μm-thick CrN(001) layer. It exhibits a strong peak at 1330 cm^{-1}, two weaker peaks at 320 and 800 cm^{-1}, as well as a feature at 600 cm^{-1} and a shoulder around 1170 cm^{-1}. The peak at 320 cm^{-1} is attributed to longitudinal acoustic phonons. First-order Raman scattering is forbidden in a perfect NaCl structure.[55,56] Therefore, this peak indicates the presence of some point defects, likely N vacancies, that relax the selection rule. A similar one phonon acoustic peak has previously been reported for CrN (Ref. 57) at 330 cm^{-1} as well as for other NaCl-structure transition-metal nitrides such as TiN,[56] $Ti_{0.12}Sc_{0.88}N$,[58] and ScN (Ref. 59) at 320 cm^{-1}, 310 cm^{-1}, and 298 cm^{-1}, respectively.

The peaks at 800 and 1330 cm^{-1} are attributed to second-order transversal and longitudinal optical phonon modes, 2TO and 2LO, respectively, while the shoulder around 1170 cm^{-1} is likely associated with the zero slope of the LO phonon dispersion curve near the Brillouin zone edge. This interpretation is done by comparison with ScN, the most closely related transition-metal nitride which also exhibits a NaCl crystal structure and a vanishing electron density of states at the Fermi level, and for which both Raman spectra[58,59] as well as detailed calculated phonon dispersion curves[58,60] have been reported. For ScN, measured peaks at 410, 680, and 1350 cm^{-1} are in good agreement with calculated TO(X) at 415 cm^{-1}, LO(L) at 657 cm^{-1}, and 2LO(L), while the calculated LO(X) at 569 cm^{-1} has not been detected experimentally, likely due to weak intensity. In direct correspondence, the 1330 cm^{-1} peak for CrN is associated with 2LO(L), the 1170 cm^{-1} shoulder with 2LO(X), and the 800 cm^{-1} peak with 2TO(X). Thus, we determine the vibrational frequencies for LO(L), LO(X), and TO(X) to be 19.9 THz, 17.5 THz, and 12.0 THz, respectively, or the corresponding phonon energies to be 82.5 meV, 72.5 meV, and 49.6 meV, respectively. The additional weak feature around 600 cm^{-1} may be attributed to a broadband of 2A and/or A+O modes. The fact that the 2LO peak is considerably more intense than the first-order Raman features attests to the excellent crystalline quality of our CrN layers. In contrast, previous studies on CrN (Ref. 57) and ScN (Ref. 59) have reported comparable Raman intensities for the (forbidden) first-order and second-order scattering, indicating a larger defect concentration than for our layers.

IV. DISCUSSION

In this section, we discuss first the electronic structure of CrN using the presented optical data in the 0.1–5 eV range,

and second the vibrational modes which dominate the optical properties in the infrared below $\hbar\omega=0.1$ eV.

The most dominant features of the CrN optical spectra in the energy range where electronic interband transitions dominate are the relatively high transmission for $\hbar\omega<0.6$ eV, a steep absorption onset at 0.64 eV, and ε_2 peaks at 1.5 eV and 2.9 eV. In order to attribute these features to specific interband transitions, we refer to reported CrN band-structure calculations[27,61] with particular emphasis on the recent calculations by Herwadkar *et al.*,[28] who showed that Coulomb interactions in the relatively flat Cr *d* bands considerably affect the overall band structure and result in the opening of an energy gap. They added a Hubbard Coulomb term $U=3-5$ eV and found that both the distorted AFM $[110]_2$ and AFM $[110]_1$ as well as the cubic FM phase form an approximately 0 eV indirect gap (depending on phase and U value) while the smallest direct transitions are slightly below 1 eV for all three cases.[28] Taking the FM CrN band structure with $U=5$ eV as an example, the gap at the Γ point between the N $2p$-like valence band and majority spin e_g conduction band is 0.7 eV and could explain the observed onset of optical absorption at 0.64 eV in our measurements, since these two bands are nearly parallel along $\Delta(\Gamma\rightarrow X)$ near the Γ point. In the same band structure, the gap between minority p-like valence band and minority spin t_{2g} band at the X point is 1.8 eV, which likely corresponds to a high joint density of states which may be responsible for the ε_2 peak that we observe at 1.5 eV. For the same electronic structure, the calculated gap between majority spin p-like valence band and majority spin t_{2g} band at the X point is 2.7 eV, which may explain the ε_2 peak or shoulder that we observe at 2.9 eV.

Our optical measurements appear, therefore, consistent with the band structure of ferromagnetic CrN with a relatively large Coulomb interaction of 5 eV. Our own measurements as well as measurements from other researchers[20–25] indicate, however, that CrN exhibits no ferromagnetic ordering. Nevertheless, the calculated ferromagnetic band structure better describes the paramagnetic NaCl-structure CrN phase than nonspin-polarized "paramagnetic" calculations, since the ferromagnetic calculations correctly predict the expected local magnetic moments. There is general consensus that CrN exhibits local magnetic moments[27,28] which were determined by neutron scattering to be $2.36\mu_B$ (Ref. 23) or $3.17\mu_B$ (Ref. 24) per Cr atom. The local magnetic moments are primarily responsible for the band splitting[27] and the related depletion of the density of states at the Fermi level and the associated reported resistivity which shows in some cases semiconductor behavior.[16,17,28] Therefore, in order to correctly interpret the interband transitions in our paramagnetic CrN, the presence of local moments in the electronic structure is more important than the correct magnetic ordering. In the absence of a true paramagnetic calculation, there is no obvious argument if the ferromagnetic or antiferromagnetic phase better predicts the experimental paramagnetic phase. We chose in our interpretation first the ferromagnetic phase, because it exhibits the correct lattice symmetry, that is, the primitive unit cell is a single Cr-N formula unit.

In order to estimate the value of the fundamental indirect gap (or overlap) between the valence-band maximum, which is approximately in the middle between Γ and K points, and the conduction-band minimum at the X point, we start with the calculated ferromagnetic band structure with $U=5$ eV which exhibits a −0.29 eV indirect band gap, where the negative sign indicates that this band structure actually exhibits a band overlap. Then, we use rigid band shifting so that the optical features at 0.64, 1.5, and 2.9 eV exactly match the direct transitions at Γ, X(minority), and X(majority), as proposed above. This results in three estimated values for the band gap of −0.35 eV, −0.6 eV, and −0.1 eV, respectively, with an average value of -0.35 ± 0.20 eV (that is, a 0.35 eV band overlap). This average was obtained by giving double weight to the transition at the Γ point, since it is expected to have the smallest uncertainty. A corresponding analysis with the calculated band structures at Γ, M, and X for the antiferromagnetic phases with $U=3$ eV and 5 eV for $[110]_1$ and $[110]_2$ phases, respectively, yields gap values of 0.68, −0.1, and 0.2 eV for the $[110]_1$ phase and 0.34, 0.6, and 0.9 eV for the $[110]_2$ phase, resulting in average band gap values of 0.36 ± 0.33 and 0.55 ± 0.23 eV for the two AFM phases. As discussed above, it is unclear which of the three magnetically ordered phases best represents the paramagnetic CrN phase. Therefore, we average over all nine values ranging from a 0.6 eV overlap to a 0.9 eV gap, give again double weight to the most reliable values associated with transitions at the Γ point, and obtain an estimated indirect band gap of NaCl-structure CrN of 0.19 ± 0.46 eV

The following discussion focuses on the dielectric function in the infrared range. We attribute the strong resonance shown in Fig. 4 to lattice vibrations, since free carrier contributions cannot explain this feature. In particular, applying a Drude free-electron model to the reflection spectrum in Fig. 2(a) for $\lambda=4-30$ μm yields no satisfactory fit, especially for $\lambda>23.4$ μm where the measured R decreases. Therefore, in the following we assume that free-carrier effects can be neglected for the entire measurement range, which corresponds to an estimated upper bound for the free-carrier density of 3×10^{19} cm^{-3}, determined using a plasma frequency of $\hbar\omega_p=0.04$ eV, an effective mass equal to the free-electron mass, and an estimated $\varepsilon=30$ for screening by valence electrons. The dielectric function in the infrared is then expressed by[52]

$$\varepsilon=\varepsilon_1+i\varepsilon_2=\varepsilon_\infty+\frac{(\varepsilon_{dc}-\varepsilon_\infty)\omega_0^2}{(\omega_0^2-\omega^2-i\gamma\omega)}, \quad (1)$$

where ε_{dc} and ε_∞ are the static (dc) and the high-frequency dielectric constants, ω_0 is the vibrational resonance frequency where ε_2 reaches the maximum, and γ is a damping term. Simultaneous fitting of the measured ε_1 and ε_2 for $0.05<\hbar\omega<0.6$ eV using Eq. (1) indicates that the dielectric function is well described with such a single vibrational mode, confirming the absence of free-carrier effects and provides values for $\hbar\omega_0=48.7\pm0.2$ meV and $\hbar\gamma=6.7\pm0.5$ meV, as well as $\varepsilon_{dc}=53\pm5$ and $\varepsilon_\infty=22\pm2$.

In the absence of free-carrier effects, CrN is described as an ionic crystal for which the Lyddane-Sachs-Teller relation provides the relationship between longitudinal and transver-

sal optical phonon frequencies ω_{LO} and ω_{TO} at the zone center Γ

$$\frac{\omega_{LO}(\Gamma)}{\omega_{TO}(\Gamma)} = \sqrt{\frac{\varepsilon_{dc}}{\varepsilon_{\infty}}}. \quad (2)$$

The measured resonance frequency corresponds to the transversal optical mode, thus $\hbar\omega_{TO}=\hbar\omega_0=48.7$ meV. Using this value as well as ε_{dc} and ε_{∞} from above, we obtain with Eq. (2) $\hbar\omega_{LO}=75.6\pm6.8$ meV, and corresponding vibrational frequencies at the Γ point of 11.7 THz and 18.2 THz for transversal and longitudinal optical modes, respectively. These values for the zone center are close to the vibrational frequencies at the zone edge, obtained from the Raman analysis. In particular, the transverse optical frequency at Γ (11.7 THz) is just 2% smaller than at the X point (12.0 THz) while the longitudinal mode at Γ (18.2 THz) is between 17.5 THz and 19.9 THz at X and L points, respectively.

The Born effective charges Z_{Cr} and Z_N are determined from the phonon optical frequencies using[62,63]

$$\omega_{LO}^2 - \omega_{TO}^2 = \frac{e^2}{\varepsilon_0\varepsilon_{\infty}V_0}\left(\frac{Z_{Cr}^2}{M_{Cr}} + \frac{Z_N^2}{M_N}\right), \quad (3)$$

where $Z_{Cr}+Z_N=0$, M_{Cr} and M_N are the masses of Cr and N ions, respectively, and V_0 is the volume of the primitive unit cell. We find $Z_{Cr}=-Z_N=4.4\pm0.9$, which is larger than the corresponding nominal charges of +3 and −3 for Cr and N ions, respectively, indicating that there is a considerable contribution due to the polarization of valence electrons.[63,64] That is, ionic displacement causes charge transfer which is facilitated by strong hybridization between N $2p$ and Cr $3d$ orbitals, similar to what has been reported, for example, between Ti and O in $BaTiO_3$.[65] This experimental evidence for hybridization supports predictions by band-structure calculations which found the highest occupied band in CrN to exhibit strong hybridization, with N $2p$ and Cr $3d$ characters near Γ and X points, respectively.[28]

The here discussed vibrational modes in CrN show resemblance to the reported modes in ScN,[58,60] which is a transition-metal nitride that has three electrons less per formula unit than CrN, but the same NaCl crystal structure with a 8.1% larger lattice constant. For example, the here measured $\upsilon_{TO}=11.7$ THz and $\upsilon_{LO}=18.2$ THz, at the zone center for CrN, are comparable to *ab initio* predicted values for ScN of 10.9 THz and 18.9 THz from Ref. 60 or 10.0 THz and 19.2 THz from Ref. 58, respectively. Similarly, our value of 4.4 for the Born effective charge for CrN is comparable to 4.04,[60] the value reported for ScN, or 4.23, the value that we calculate from the reported vibrational frequencies of ScN.[58] In contrast, TiN exhibits considerably different vibrational modes than CrN. It has the same NaCl structure as CrN, with a 0.5% larger lattice constant, but exhibits metallic conductivity which facilitates screening so that TO and LO branches at the Γ point are degenerate at 17.3 THz (Ref. 58) and the Born effective charge for TiN is zero. We attribute the similarity of CrN and ScN to the negligible density of states at the Fermi level for both materials. ScN has completely filled N $2p$ and empty Sc $3d$ bands (here, for terminology purposes only, hybridization is neglected) resulting in an indirect band gap of ~1.3 eV.[32] CrN has three electrons per formula unit more. They form local magnetic moments and are expected to completely fill the three Cr $3d$ bands with primarily t_{2g} symmetry for one spin direction. They also increase the dielectric constant, as evident from our measured $\varepsilon_{dc}=53$ and $\varepsilon_{\infty}=22$ for CrN, which are considerably larger than $\varepsilon_{dc}=38$ and $\varepsilon_{\infty}=12$ for ScN.[60] If the band splitting due to the local moments is sufficient, CrN also exhibits a band gap, as suggested by ferromagnetic and antiferromagnetic calculations which include an interaction term.[28] Our measured vibrational modes for CrN and their similarity to ScN suggest that this is actually the case, that is, CrN exhibits a band gap.

V. CONCLUSION

Single crystal CrN(001) layers, 44 to 11,000 nm thick, were deposited on MgO(001) by ultrahigh vacuum magnetron sputtering at a growth temperature of 700 °C. XRD ω-2θ, ω rocking curves, and φ scans show that the films have a very good crystalline quality with a cube-on-cube epitaxial relationship with the substrate, $(001)_{CrN}\|(001)_{MgO}$ and $[001]_{CrN}\|[001]_{MgO}$.

Reflectance and transmittance spectra are measured in the wavelength range from 250 nm−30 μm using a spectrophotometer and an FTIR spectrometer. CrN optical constants, n and k are determined using an iterative procedure which takes advantage of the absorption in the bulk of the layers and is therefore relatively insensitive to surface oxidation and roughness, and sample thickness nonuniformity, as well as errors in correctly accounting for interference effects, and is complemented by a Kramers-Kronig analysis for $\lambda > 3$ μm. The CrN refractive index continuously increases from $n=2.7$ at $\lambda=250$ nm to a peak of $n=5.7$ at $\lambda=840$ nm, followed by a nearly constant value of $n=5.2$ between $\lambda=1.2$ and 6.2 μm and a peak in the infrared where n reaches 12.4 at $\lambda=26.6$ μm. The absorption coefficient shows a sharp increase above $\hbar\omega=0.64$ eV and the imaginary part of the dielectric function exhibits a peak at $\hbar\omega=1.5$ eV and a shoulder at $\hbar\omega=2.9$ eV. These three energies correspond to direct electronic interband transitions which are associated with predicted gaps at high-symmetry points in the Brillouin zone for ferromagnetic and antiferromagnetic cubic CrN phases, which more accurately describe the electronic structure of paramagnetic CrN than nonspin-polarized calculations. A direct comparison of gap values and optical transition energies provides an estimate for the CrN band gap of 0.19 ± 0.46 eV.

Analysis of the dielectric constant in the long-wavelength range provides values for the zone-center optical phonon frequencies $\upsilon_{TO}=11.7$ THz and $\upsilon_{LO}=18.2$ THz, and low- and high-frequency dielectric constants $\varepsilon_{dc}=53$ and $\varepsilon_{\infty}=22$. The large separation between transverse and longitudinal optical phonon modes at the Γ point is related to an anomalous large value of the Born effective charge of 4.4, which is attributed to a strong hybridization of Cr $3d$ and N $2p$ orbitals. The CrN Raman spectrum is dominated by second-order peaks at 800 cm^{-1}, 1170 cm^{-1}, and 1330 cm^{-1} that are associated with 2TO(X), 2LO(X), and 2LO(L) modes, respectively, and confirm the vibrational frequencies obtained from the reflec-

tance measurements. In addition, there is a first-order acoustic phonon peak at 320 cm^{-1}.

In summary, electronic interband transitions as well as vibrational modes in CrN, studied by optical spectroscopy for $\hbar\omega$ above and below 0.1 eV, respectively, suggest a strong depletion of the density of states at the Fermi level and likely the presence of an indirect band gap. This is attributed to the formation of local magnetic moments and electron interaction effects, indicating that CrN is likely a Mott-Hubbard-type insulator.

ACKNOWLEDGMENTS

This research was supported by the National Science Foundation under Grant No. 0645312.

[1] P. Panjan, B. Navinšek, A. Cvelbar, I. Milošev, and A. Zalar, Thin Solid Films **281-282**, 298 (1996).
[2] P. Hones, C. Zakri, P. E. Schmid, F. Lévy, and O. R. Shojaei, Appl. Phys. Lett. **76**, 3194 (2000).
[3] I. Milošev, J. M. Abels, H.-H. Strehblow, B. Navinšek, and M. Metikoš-Huković, J. Vac. Sci. Technol. A **14**, 2527 (1996).
[4] J. Stockemer, R. Winand, and P. V. Brande, Surf. Coat. Technol. **115**, 230 (1999).
[5] C. P. Constable, J. Yarwood, P. Hovsepian, L. A. Donohue, D. B. Lewis, and W.-D. Münz, J. Vac. Sci. Technol. A **18**, 1681 (2000).
[6] C. P. Mulligan and D. Gall, Surf. Coat. Technol. **200**, 1495 (2005).
[7] C. P. Mulligan, T. A. Blanchet, and D. Gall, Surf. Coat. Technol. **204**, 1388 (2010).
[8] P. A. Anderson, R. J. Kinsey, S. M. Durbin, M. Markwitz, J. Kennedy, A. Asadov, W. Gao, and R. J. Reeves, J. Appl. Phys. **98**, 043903 (2005).
[9] A. Ney, R. Rajaram, S. S. P. Parkin, T. Kammermeier, and S. Dhar, Appl. Phys. Lett. **89**, 112504 (2006).
[10] A. Ney, R. Rajaram, S. S. P. Parkin, T. Kammermeier, and S. Dhar, Phys. Rev. B **76**, 035205 (2007).
[11] P. Subramanya Herle, M. S. Hegde, N. Y. Vasathacharya, S. Philip, M. V. Rama Rao, and T. Sripathi, J. Solid State Chem. **134**, 120 (1997).
[12] P. Panjan, B. Navisek, A. Cvelbar, A. Zalar, and J. Vlcek, Surf. Coat. Technol. **98**, 1497 (1998).
[13] K. K. Shih, D. B. Dove, and J. R. Crowe, J. Vac. Sci. Technol. A **4**, 564 (1986).
[14] M. Cekada, P. Panjan, B. Navinsek, and F. Cvelbar, Vacuum **52**, 461 (1999).
[15] R. Mientus and K. Ellmer, Surf. Coat. Technol. **116-119**, 1093 (1999).
[16] D. Gall, C.-S. Shin, R. T. Haasch, I. Petrov, and J. E. Greene, J. Appl. Phys. **91**, 5882 (2002).
[17] C. Constantin, M. B. Haider, D. Ingram, and A. R. Smith, Appl. Phys. Lett. **85**, 6371 (2004).
[18] K. Inumaru, K. Koyama, N. Imo-oka, and S. Yamanaka, Phys. Rev. B **75**, 054416 (2007).
[19] C. X. Quintela, F. Rivadulla, and J. Rivas, Appl. Phys. Lett. **94**, 152103 (2009).
[20] J. D. Browne, P. R. Liddell, R. Street, and T. Mills, Phys. Status Solidi A **1**, 715 (1970).
[21] Y. Tsuchiya, K. Kosuge, Y. Ikeda, T. Shigematsu, S. Yamaguchi, and N. Nakayama, Mater. Trans., JIM **37**, 121 (1996).
[22] D. Gall, C.-S. Shin, T. Spila, M. Odén, M. J. H. Senna, J. E. Greene, and I. Petrov, J. Appl. Phys. **91**, 3589 (2002).
[23] L. M. Corliss, N. Elliott, and J. M. Hastings, Phys. Rev. **117**, 929 (1960).
[24] R. M. Ibberson and R. Cywinski, Physica B **180-181**, 329 (1992).
[25] M. N. Eddine, F. Sayetat, and E. F. Bertaut, C. R. Seances Acad. Sci., Ser. B **269**, 574 (1969).
[26] F. Rivadulla, M. Banobre-Lopez, C. X. Quintela, A. Pineiro, V. Pardo, D. Baldomir, M. A. Lopez-Quintela, J. Rivas, C. A. Ramos, H. Salva, J. S. Zhou, and J. B. Goodenough, Nature Mater. **8**, 947 (2009).
[27] A. Filippetti, W. E. Pickett, and B. M. Klein, Phys. Rev. B **59**, 7043 (1999).
[28] A. Herwadkar and W. R. L. Lambrecht, Phys. Rev. B **79**, 035125 (2009).
[29] A. Filippetti and N. A. Hill, Phys. Rev. Lett. **85**, 5166 (2000).
[30] A. R. Smith, H. A. H. Al-Brithen, D. C. Ingram, and D. Gall, J. Appl. Phys. **90**, 1809 (2001).
[31] C.-S. Shin, D. Gall, Y.-W. Kim, P. Desjardins, I. Petrov, J. E. Greene, M. Odén, and L. Hultman, J. Appl. Phys. **90**, 2879 (2001).
[32] D. Gall, M. Städele, K. Järrendahl, I. Petrov, P. Desjardins, R. T. Haasch, T.-Y. Lee, and J. E. Greene, Phys. Rev. B **63**, 125119 (2001).
[33] C. P. Mulligan, T. A. Blanchet, and D. Gall, Surf. Coat. Technol. **203**, 584 (2008).
[34] J. M. Purswani, T. Spila, and D. Gall, Thin Solid Films **515**, 1166 (2006).
[35] X. Y. Zhang and D. Gall, Thin Solid Films **518**, 3813 (2010).
[36] J. R. Frederick, J. D'Arcy-Gall, and D. Gall, Thin Solid Films **494**, 330 (2006).
[37] D. Gall, I. Petrov, L. D. Madsen, J.-E. Sundgren, and J. E. Greene, J. Vac. Sci. Technol. A **16**, 2411 (1998).
[38] O. Stenzel, *The Physics of Thin Film Optical Spectra: An Introduction* (Springer, Berlin, 2005).
[39] Edward D. Palik, *Handbook of Optical Constants of Solids II* (Academic Press, San Diego, CA, 1991).
[40] C. Kittel, *Introduction to Solid State Physics*, 7th ed. (Wiley, Hoboken, NJ, 1995).
[41] D. L. Greenaway and Gunther Harbeke, *Optical Properties and Band Structure of Semiconductors* (Pergamon Press, Long Island, NY, USA, 1968).
[42] O. Madelung, U. Rössler, and M. Schulz, *Semiconductors: II-VI and I-VII Compounds*, Landolt-Börnstein—Group III Condensed Matter, Vol. 41B (Springer-Verlag, Berlin, 1999).
[43] The value for a_{MgO}=4.213 Å is from the inorganic index to powder diffraction (Joint Committee on Powder Diffraction Standards, International Center for Powder Diffraction Data,

Newtown Square, PA, 1998): MgO (Card No. 04-0829).
[44] P. Hones, M. Diserens, R. Sanjines, and F. Levy, J. Vac. Sci. Technol. B **18**, 2851 (2000).
[45] P. M. Fabis, R. A. Cooke, and S. McDonough, J. Vac. Sci. Technol. A **8**, 3819 (1990).
[46] The value for a_{CrN}=4.14 Å is from the inorganic index to powder diffraction (Joint Committee on Powder Diffraction Standards, International Center for Powder Diffraction Data, Newtown Square, PA, 1998): CrN (Card No. 11-0065, 76-2494).
[47] J. R. Frederick and D. Gall, J. Appl. Phys. **98**, 054906 (2005).
[48] J. R. Frederick and D. Gall, Appl. Phys. Lett. **87**, 053107 (2005).
[49] H.-S. Seo, T.-Y. Lee, J. G. Wen, I. Petrov, J. E. Greene, and D. Gall, J. Appl. Phys. **96**, 878 (2004).
[50] C.-S. Shin, S. Rudenja, D. Gall, N. Hellgren, T.-Y. Lee, I. Petrov, and J. E. Greene, J. Appl. Phys. **95**, 356 (2004).
[51] C.-S. Shin, Y.-W. Kim, N. Hellgren, D. Gall, I. Petrov, and J. E. Greene, J. Vac. Sci. Technol. A **20**, 2007 (2002).
[52] M. Born and K. Huang, *Dynamical Theory of Crystal Lattices* (Oxford University Press, London, UK, 1954).
[53] K. Hisano, F. Placido, A. D. Bruce, and G. D. Holah, J. Phys. C **5**, 2511 (1972).
[54] J. C. Willmott, Proc. Phys. Soc., London, Sect. A **63**, 389 (1950).
[55] G. P. Montgomery, Jr., M. V. Klein, B. N. Ganguly, and R. F. Wood, Phys. Rev. B **6**, 4047 (1972).
[56] W. Spengler, R. Kaiser, A. N. Christensen, and G. Muller-Vogt, Phys. Rev. B **17**, 1095 (1978).
[57] A. Barata, L. Cunha, and C. Moura, Thin Solid Films **398-399**, 501 (2001).
[58] D. Gall, M. Stoehr, and J. E. Greene, Phys. Rev. B **64**, 174302 (2001).
[59] G. Travaglini, F. Marabelli, R. Monnier, E. Kaldis, and P. Wachter, Phys. Rev. B **34**, 3876 (1986).
[60] T. R. Paudel and W. R. L. Lambrecht, Phys. Rev. B **79**, 085205 (2009).
[61] D. A. Papaconstantopoulos, W. E. Pickett, B. M. Klein, and L. L. Boyer, Phys. Rev. B **31**, 752 (1985).
[62] K.-W. Lee and W. E. Pickett, Phys. Rev. B **68**, 085308 (2003).
[63] R. Resta, M. Posternak, and A. Baldereschi, Phys. Rev. Lett. **70**, 1010 (1993).
[64] R. M. Pick, M. H. Cohen, and R. M. Martin, Phys. Rev. B **1**, 910 (1970).
[65] Ph. Ghosez, X. Gonze, Ph. Lambin, and J.-P. Michenaud, Phys. Rev. B **51**, 6765 (1995).